# Bias-Switchable Photodetector From Broadband to UV-Selective Detection Mode Leveraging Nanolayered Dual-Schottky Junction

Hyeonghun Kim<sup>a,#</sup>, Molly Rothschild<sup>a</sup>, Dong Hun Lee<sup>a</sup>, Chung Soo Kim<sup>b</sup>, Jeongmin Park<sup>b</sup>, Byung-Cheol Min<sup>c</sup>, Sunghwan Lee<sup>\*a</sup>

<sup>a</sup>School of Engineering Technology, Purdue University, West Lafayette, IN 47907, USA.

<sup>b</sup>Analysis Technical Center, Korea Institute of Ceramic Engineering and Technology, Jinju, Gyeongsangnam-do 52851, Republic of Korea.

<sup>c</sup>Department of Computer and Information Technology, Purdue University, West Lafayette, IN 47907, USA.

KEYWORDS. photodetectors, dual-Schottky junction, broadband photodetectors, visible-blind UV photodetectors, dual-mode detection

\*present address: Ceramics Test-Bed Center, Korea Institute of Ceramic Engineering and Technology, Icheon, Gyeonggi-do 17303, Republic of Korea

\*corresponding authors: sunghlee@purdue.edu

#### Abstract

The limitless potential of ultraviolet (UV) information is fueling the development of photodetecting technology beyond color image acquisitions such as air pollution monitoring, oil spill detection, and missile tracking systems. Ideal detectors for such applications need to separately perceive UV and visible lights to maximize their functional versatility. However, traditional device structures (e.g., photodiodes and photoconductors) inevitably require expensive filters or supplementary devices to discriminate the light sources. This study aims to develop photodetectors that provide dual functionalities in a single-unit device without any filters. To this end, we propose a device configuration based on two Schottky diodes stacked in antiparallel. The dual Schottky junctions (DSJs) uniquely arrange the band structure within the device to selectively create photocurrent from the targeted wavelengths (UV/visible) of light and block the rest (visible/UV) by adjusting the bias polarity. In addition, we further demonstrate dual-spectral detection in real-time by mapping UV and broadband (UV+visible) light images in a single frame without the aid of supplementary filters or equipment. The filter-free system, capable of UV/visible discrimination, would pave the way for developing a universal and multimodal next-generation photodetector with enhanced detection rates.

#### 1. Introduction

Photodetectors, recording light information in the form of electrical signals, play pivotal roles in high-end technologies such as image sensing, motion tracking, and bio-sensing.<sup>1,2</sup> Silicon (Si) has been a basic building block of the most commercially available photodetectors, capable of responding to visible (400-700 nm) and near-infrared light (700-1100 nm) owing to the superior compatibility with the existing integrated circuits (IC).<sup>3,4</sup> However, the progress relying on Si is encountering limitations in expanding their target wavelength. In particular, despite the increasing demands in a wide range of applications, such as fire monitoring, oil spill detection, and missile tracking systems, Si-based photodetectors have been lacking of required UV sensitivity due to the short penetration depth of the light (< 20 nm) and the consequent light dead region in conventional Si devices.<sup>5-7</sup>

To establish high-performance UV detecting technologies, engineers are now paying attention to wide-bandgap (WB) semiconductors. Among them, metal oxides (e.g., ZnO, Ga<sub>2</sub>O<sub>3</sub>, SnO<sub>2</sub>, or In<sub>2</sub>O<sub>3</sub>) are promising candidates due to their high excitation binding energy, affordable fabricating process, and chemical stability.<sup>5–7</sup> Numerous UV photodetectors integrating these WB semiconductors have been fabricated in the form of PN, Schottky diodes, and photoconductors, demonstrating much enhanced UV sensitivity compared to traditional Si-based detectors.<sup>6,8–10</sup> Another notable feature of those WB-based devices is their visible-blind UV detection which selectively tracks UV sources without interference from sunlight or artificial visible light.<sup>5,6,10</sup>

Meanwhile, broadband detectors, sensitive to both UV and visible lights, have also been extensively developed to expand the versatility of photo-detecting systems. 11,12 Although the non-selective nature of them requires an aid of supplementary bandpass filters to separately

encode UV information, their functionality can be tailored for the sake of desired purposes.<sup>11</sup> The most intuitive and affordable way to construct the broadband detectors is to combine the WB semiconductors with narrow-bandgap (NB) materials (e.g., Si, perovskite, or MoS<sub>2</sub>).<sup>13–20</sup> For example, a device configuration in the form of a PN diode, consisting of n-type WB and p-type NB semiconductors, has been adopted in many studies as a basic building block for drawing a broad spectral response.<sup>13–18</sup> Heterogeneous mixtures of WB and NB semiconductors have also been exploited to secure the broadband characteristic and exceptional photoconductive gain up to  $10^4$ .<sup>19,20</sup>

However, despite accumulated advances in UV detectors, all existing approaches face inherent limitations when mapping visible and UV images in a single frame, particularly required for applications such as air-pollution monitoring, fire monitoring, oil spill detection, and missile tracking systems where both visible and UV information play a critical role.<sup>6,10,21</sup> For this purpose, broadband detectors must be equipped with bandpass filter arrays consisting of two types of pixels that can selectively transmit visible light and ultraviolet light respectively.<sup>22,23</sup> But, the alignment process for the filter with devices requires costly manufacturing steps and adds processing complexities.<sup>22,23</sup> Although visible-blind detectors can selectively observe UV light without filters, it requires the support of supplementary detectors to obtain information from visible light. Therefore, a novel detector, which enables selective discrimination of UV information from visible light noise without an additional filter or device, needs to be contrived.

As the most intuitive solution to the limitations above, novel photodetectors, whose spectral responses are reversibly switchable depending on the polarity of the external electric field, have been contrived. Among them, PN diodes, leveraging a metal oxide layer as UV-absorber on a Si wafer as visible absorber, have been considered to discriminate UV/visible light

without filter and multiple device arrays.<sup>24-26</sup> Although the devices respond to a broadband illumination (UV and visible) under reverse bias through a photovoltaic (PV) effect, their spectral response becomes UV-selective at the opposite bias condition. The latter sensing mode is driven by the photoconductive (PC) mechanism, accompanying the conductivity change of the metal oxide layer. However, the PC mechanism always faces a critical limitation in detection rate, correlated with a sluggish O<sub>2</sub> adsorption/desorption process.<sup>24-26</sup> Thus, to mitigate the slow detection rate, an innovative device architecture is to be designed to accelerate the photo detecting speed while maintaining the desired mode-tunable characteristics.

Herein, we suggest a double Schottky junction (DSJ) detector as a breakthrough approach to realizing broadband and visible-blind functionalities in a single device. The suggested device consists of two Schottky junctions by stacking n-type IGZO (InGaZnO)/PEDOT (poly-3,4-ethylene dioxythiophene doped with polystyrene sulfonate) and PEDOT/n-type Si diodes, of which the internal-electric fields are created in the opposite direction to each other. The antiparallel (or back-to-back diode) configuration allows the device's functionality to switch from broadband detecting to visible-blind UV detecting mode by adjusting the direction of the external voltage bias. It should be noted that, contrary to existing bias-tunable detectors relying on the sluggish photocatalytic process, the suggested DSJ device is advantageous in detecting speed since the detection rate is dominated by rapid photovoltaic charge generation driven in the Schottky junction between the IGZO/PEDOT layer. Besides, we present a new strategy to further accelerate the detection rate by introducing a pulse biasing system, which enables simultaneous dual-mode detection of broadband detection and selective UV extraction without additional filters. This unique concept is expected to be a game changer for the next-generation UV detector

industry in that it provides a foundation to address the inherent limitations of existing broadband and visible-blind UV detectors with enhanced detection rates.

#### 2. Experimental Section

#### 2.1. Device fabrication

A dry-oxidized silicon wafer (<100>, n-type, the resistivity of 1-10  $\Omega$  cm, University Wafer) with a 100 nm-thick oxide layer was cleaned using acetone and isopropyl alcohol (VWR) in sequence. After the cleansing process, an active area (2×2 mm<sup>2</sup>) was patterned on the Si wafer by using photolithography and etching process based on a BOE solution. A Poly(3,4-ethylene dioxythiophene) polystyrene sulfonate (PEDOT, PH1000, Ossila) film was spin-casted on the wafer of which the surface was pre-treated using oxygen plasma (PDC-001, Harrick Plasma). After a thermal stabilization of the polymer at 150°C for 10 min, a 5 nm-thick of MoO<sub>3</sub> layer was deposited using a thermal evaporator (JV18EVA-F30k2p, JVAC). As a second photoactive layer, an IGZO film was formed on the sample, using an RF magnetron sputtering system (JV19MS-P24H4, JVAC). The deposition pressure was adjusted as a constant pressure of 2 mTorr with a 5% O<sub>2</sub> gas, diluted in Ar. The pre-deposited film was thermally stabilized on a hot plate at 250°C for 30 min. Finally, the fabrication was completed after depositing an ITO top electrode (100 nm) and an Al bottom electrode (150 nm) by using the sputtering system and thermal evaporator, respectively. The Al (conductivity<sup>27</sup> of 3.3×10<sup>7</sup> S m<sup>-1</sup> and work function<sup>28</sup> of 4.3 eV) was chosen by considering high conductivity, and a relatively low Schottky junction between the n-Si (work function of 4.1-4.2 eV). All fabrication steps and relevant device architectures were visualized in Figure S1a (Supporting Information). The photo and microscopic images of the completed device were in Figure S1b and c (photo and microscope images).

#### 2.2. Materials and device characterization

The thickness of each layer was analyzed using an Ellipsometer (FilmSense FS-1). Cross-sectional transmission electron microscopy (TEM) analysis was conducted using a Themis Z (FEI). The TEM sample was prepared based on a focused ion beam (FIB, Helios G4 UC DualBeam system, Thermo scientific) process. The optical reflectance was measured using a UV-visible spectrometer, equipped with an attenuated total reflectance accessory (Lambda 950). The opto-electrical performances were measured using an Agilent 4155B under the illumination of LEDs (Mightex). Rise and decay times were precisely measured using an oscilloscope (Hantek, DSO4254B) at a constant AC voltage, controlled by Keithley 2400.

#### 3. Results and discussion

#### 3.1. Characterization of the DSJ device

The pivotal building blocks for the DSJ are two n-type semiconductors and a high work-function material (Figure 1a) where the high work function is required to form two back-to-back Schottky junctions with large built-in potentials on both sides. In this research, Si and IGZO were exploited as the photoactive n-type semiconductors while PEDOT was intercalated between the two n-type materials as the high work function material. An ultrathin MoO<sub>3</sub> (~5 nm), of which the work function (5.0-5.2 eV)<sup>29-32</sup> is well-matched with that of the PEDOT (~5.1 eV),<sup>33,34</sup> was additionally deposited to protect the PEDOT layer from a high energy sputtering process. Indium-tin oxide (ITO) and aluminum (Al) were employed as top and bottom electrodes, respectively. Through literature surveys, the band alignments of the DSJ diode were estimated as shown in Figure 1b.<sup>29-37</sup> The Fermi-level difference between the PEDOT layer and the n-type semiconductors creates two distinctive Schottky junctions, their built-in potentials were 0.45 eV (*Esb1*, Si/PEDOT junction) and 0.5 eV (*Esb2*, IGZO/PEDOT junction), respectively. The junction

between IGZO and ITO has a much lower barrier height (0.1-0.15 eV) than the Schottky junctions, which has little effect on the optoelectrical properties of the device. Therefore, it can be assumed that the two Schottky junctions are the dominant factors determining the characteristics of the device. The formation of the Schottky junctions was directly proved by fabricating PEDOT/Si and PEDOT/IGZO diodes as shown in Figure S2 (Supporting Information).

The light-trapping capability of the device was simulated using the transfer matrix method.<sup>38</sup> Figure 1c demonstrates optical field profiles within a virtual device, composed of ITO (100 nm) / IGZO (300 nm) / MoO<sub>3</sub> (5 nm) / PEDOT (50 nm) / Si (500  $\mu$ m) / Al (1500 nm), under various monochromatic lights from 300 to 700 nm. The illumination orientation was set in the direction from ITO to Si (from bottom to top in Figure 1c). The rationality of the numerical analysis was confirmed by comparing the theoretical and empirical reflectance of the device as shown in Figure S3 (Supporting Information). Based on the simulated results, the charge generation rate ( $C_G$ ) was calculated as follows (Figure 1d):

$$C_G = \frac{2\pi\varepsilon_0 nk}{h} \|\mathbf{E}\|^2 \tag{1}$$

where n and k are the real and imaginary parts of the complex refractive index of the layer and E is the optical field. The permittivity of free space,  $\varepsilon_0$  and the Planck constant, h are also related to the  $C_G$  equation. Below 370 nm wavelength light, of which the single-photon energy matches with the bandgap of IGZO (~3.3 eV), $^{35-37}$  the photo-induced charge generation dominantly occurred in the IGZO layer. In contrast, the  $C_G$  values of the ITO/IGZO/PEDOT/MoO<sub>3</sub> layers under visible light (wavelength > 370 nm) were negligible, while its intensity was suddenly amplified near the Si/PEDOT boundary. These  $C_G$  distribution results in Figure 1d represent that UV and visible lights are mainly absorbed in the IGZO and Si layers, respectively.

To explore the effects of the IGZO layer in more detail, the  $C_G$  under the illumination of UV light (300-400 nm) was investigated by varying the thickness of the IGZO layer (Figure 1e and 1f). The  $C_G$  distribution of the IGZO layer (Figure 1e) demonstrated multiple local maximum points (LMPs; red regions) owing to interference fringes, attributed to the refractive index mismatch between heterogeneous layers. The  $C_G$  value of the most upper region of each IGZO thickness gradually decreased with increasing the thickness (Figure 1e). Eventually, with the 500-nm thick IGZO, the  $C_G$  value at the upper fringe became less than 1/10 that of the bottom LMP value, implying that most UV lights were absorbed in the bottom part of the IGZO layer. The absorption coefficient of IGZO under UV light illumination is well known in a range of 10<sup>5</sup> (cm<sup>-1</sup>), representing the optical penetration depth is about 100 nm.<sup>39,40</sup> Therefore, the number of UV photons reaching the upper region of the IGZO (i.e., bottom region of the IGZO in the schematic, Figue 1a) decreases dramatically when the film thickness is thicker than 100 nm. The strong UV absorptivity of the IGZO layer affects the  $C_G$  distribution of the Si layer, and it is proved from Figure 1f that the UV absorption in the Si region decreases as the IGZO layer thickness increases. As shown in Figure S4 (Supporting Information), total  $C_G$  ( $TC_G$ ) of the Si and IGZO layers were numerically calculated by integrating all  $C_G$  across the entire depth of each layer with varying the IGZO thicknesses and a fixed wavelength of 365 nm. The  $TC_G$  of the IGZO gradually increased with increasing the IGZO thickness and surpassed that of the Si as the IGZO thickness > 250 nm.

The dual-mode operations (broadband / visible-blind UV detection) demand a prerequisite condition that can equivalently distribute injected UV photons into the IGZO and Si layers. If the UV light is entirely absorbed in the IGZO layer by increasing the layer thickness, only longer wave light (i.e., visible light) would be absorbed in the Si. Therefore, UV-only and

visible-only responses are more likely to be realized. However, given that the IGZO is a much inferior photo-conductor to the single-crystalline Si due to its amorphous nature, the UV sensitivity of the DSJ device is expected to be critically insufficient for practical use. For this reason, it is necessary to compensate for the low sensitivity of IGZO by allowing some UV to be absorbed by the Si and measuring the light with higher sensitivity. On the other way, if the thickness of the IGZO is too narrow and mostly UV light penetrates the layer, the DSJ device loses the wavelength selectivity and cannot distinguish the UV from visible light anymore. In this regard, identifying a specific IGZO thickness that enables equivalent UV light distribution in Si and IGZO is the pivotal key to dual mode detection.

Besides, the photo-induced charges in the IGZO layer tend to be rapidly recombined at locations far from the Schottky junction (IGZO/PEDOT); thus, the 200-300 nm-thick of IGZO would be beneficial for improving charge collection efficiency, compared to the device with thicker IGZO layer. On the other hand, the too-thin IGZO layer could be the origin of undesired high current leakage under dark conditions; thus, we selected 300 nm-thick IGZO as the optimized thickness to limit the leakage current while maintaining high charge collection efficiency for the designed dual junction photodetector.

A high-angle annular dark-field scanning transmission electron microscopy (HAADF-STEM) image and its associated energy-dispersive X-ray spectroscopy (EDS) mapping image (Figure 2a and S5, Supporting Information) demonstrate the completed device structure consisting of ITO (100 nm) / IGZO (300 nm) / MoO<sub>3</sub> (5nm) / PEDOT (50 nm), placed on an n-type Si substrate. The ultrathin MoO<sub>3</sub> was exploited to protect the PEDOT layer from the high-energy plasma generated during the sputtering deposition (Figure S6, Supporting Information). Overall fabrication is described in the Experimental section in more detail.

The optical reflectance of the device was investigated, as shown in Figure 2b. Interference fringes were caused by the refractive index mismatch between the heterogeneous layers, which evokes an irregular reflectance fluctuation depending on the wavelength. However, the reflectance of the DSJ structure significantly decreased in the overall wavelength region, including visible and UV light, compared to that of the bare Si substrate. Particularly in the UV region, due to the fact that no significant decreases were observed in reflectance after depositing PEDOT and MoO<sub>3</sub> (Figure S7, Supporting Information), it is reasonable to assert that the reduced reflectance is attributed to the IGZO layer. Although MoO3 is well-known as an electron-blocking layer that allows only holes to pass through and effectively separates electronhole pairs at zero bias, the positive effect of the MoO<sub>3</sub> on the photovoltaic effect becomes gradually faint as the engaged bias increases due to the trap-assisted tunneling effect. 42-45 Moreover, the addition of ultra-thin MoO<sub>3</sub> (~5 nm) did not show a significant change in reflectance even in the visible range (Figue S7 in Supporting Information), which means that the optoelectric properties of the thin film had a negligible effect on the device. Consequently, we could exclude the optoelectrical influence of the MoO<sub>3</sub> layer on the DSJ device. Note that the transmittance in our device structure is assumed to be zero due to the thick bulk Si (550 µm) relative to the cumulative thickness of the rest layers (~450 nm). Thus, the IGZO layer is expected to serve as a UV-selective photo-absorber.

A current-voltage (*I-V*) curve of the DSJ device was investigated as shown in Figure 2c. While the bottom (Al) electrode was grounded, the voltages, applied on the top (ITO) electrode, were linearly swept from -5 to 5 V. The DSJ device always possessed a high-resistive zone regardless of the voltage polarity owing to the reversely aligned Schottky diodes. The device characteristic of anti-parallel configuration was revealed by not only the suppressed dark currents

at both polarities but also the weak rectifying behavior of the dark current, which was clearly distinct from conventional Schottky diodes. The photo-detecting performance of the device was explored under a monochromatic light (irradiance of 1 mW cm<sup>-2</sup>) for which 365 and 625 nm LEDs were employed as representative light sources for UV and visible light respectively (Figure 2c). The most notable feature of the device was switchable spectral response depending on the voltage polarity. First, both light sources stimulated the device to generate a photocurrent at the negative voltage (Figure 2c). In contrast, as reversing the voltage polarity to positive (+ voltage on ITO), the device revealed a photo-selectivity, which only responded to UV light (Figure 2c and 2d). It is an evident demonstration that the functionality of the device is switched from the broad-band detection to the visible-blind UV detection mode (and vice versa) by simply reversing the external bias direction. The voltage-tunability was not observable in a PEDOT-free device (Figure S8, Supporting Information), implying that leveraging the DSJ structure played a key role in the realization of multifunctional mode in a single device-based photodetector.

The spectral response was further investigated at various wavelengths of LED sources and the results are shown in Figure 2e. Two representative voltages of -2 and +5 V were selected for the negative and positive voltage conditions that result in similar dark currents (Figure 2c). The normalized spectral photocurrent at +5 V demonstrated the visible-blind UV response with a cut-off wavelength between 380-400 nm, which coincided with the bandgap of IGZO (3.3 eV). The detectable range was automatically extended by tuning the voltage to -2 V. The device became sensitive to a wide range of light sources from 350 to 700 nm owing to the contribution of narrow band Si (1.1 eV) on the photocurrent generation, which could eventually be converted into a broadband detector. These discernible differences in the response to light validate the suggested DSJ approach to establish a single device-based multimodal photodetector.

The underlying mechanism of the dual-functionality is based on the reversible change of energy-band bending with the external bias (Figures 2f and 2g). For the first case, the negative voltage (Figure 2f; applied to ITO) steepens the band bending of the Si/PEDOT junction, whereas flattening that of the IGZO/PEDOT junction. In the band alignment, only the Si has a sufficient built-in potential, enabling effective charge separation of electron-hole pairs. Upon the light injection (visible or UV light), photo-induced electrons flow toward the positively applied bottom electrode (i.e., Al), while the hole is transferred to the PEDOT layer. At this time, the IGZO serves as an electron injecting layer that supplements electrons to recombine the holes accumulated in the PEDOT layer. Based on this charge flow scheme, only photo-charges triggered by the light absorption in the Si are separated and inflow into the circuit. For the second condition with the switched bias direction (i.e., defined as the positive bias to ITO), the role of each layer is reversed (Figure 2g). The Si now becomes an electron injection layer, and the IGZO-PEDOT junction with a broader depletion region becomes photoactive to generate photoinduced charges. A distinct difference compared to the negative voltage application should be noticed: the device becomes UV-selective with the positive bias, as the larger bandgap of IGZO (3.3 eV) only allows absorption of short-wavelength (< 370 nm) photons.

As the significant figure of merit, the responsivity ( $R_{\lambda}$ ) and detectivity ( $D_{\lambda}$ ) were explored as shown in Figure S9 (Supporting Information). Both parameters at -2 V gradually increased with decreasing light irradiance and eventually became saturated when the irradiance became below 1  $\mu$ W cm<sup>-2</sup>. The maximal  $R_{\lambda}$  and  $D_{\lambda}$  (Figure S9a and c) were 1.5 A W<sup>-1</sup> and 1.9×10<sup>12</sup> Jones, respectively, which are comparable to previously reported diodes based on a heterojunction of WB semiconductor/Si.<sup>46–50</sup> The performance indices under UV light were slightly decremented at the positive voltage and even at a higher external electric field applied ( $R_{\lambda}$  of 0.16 A W<sup>-1</sup> and

 $D_{\lambda}$  of 1.4×10<sup>11</sup> Jones at + 5 V in Figure S9b and d). The depressed performance at the visible-blind mode might be attributed to the amorphous and high-defect nature of the IGZO film with an abundant charge recombination center. (Further studies with a highly crystalline and wide-bandgap semiconductor, which is expected to improve the photo-detecting performance at the positive voltage are underway.)

## 3.2. Pulsed voltage engaged detecting system for simultaneous broadband and UV-selective detection

The photoresponse rate of the device, rise and decay times under UV illumination were investigated at -2 and +5 V (Figure 3a and 3b, respectively). The device at the negative voltage (Figure 3a) reached equilibrium rapidly, within 1 ms (50 and 300 µs for the rise and decay times, respectively, Figure S10, Supporting Information). Contrary, at +5 V, the time-resolved current levels demonstrated a much slower behavior with a rise time of about 1 s and did not recover even after 10 s (Figure 3b). The undesired response/recovery delay may result from the defects in IGZO and/or at the IGZO/PEDOT hybrid interface that trap the photo-induced charges and release them at a relatively sluggish rate.<sup>51–53</sup>

One possible tactic to accelerate the charge de-trapping is to inject a negative voltage spike into the device (Figure 3c). A voltage spike is indeed found to be a working strategy to facilitate the hole migration from the PEDOT to IGZO, which leads to rapid recombination with the trapped electrons in IGZO and at the IGZO/PEDOT interface and initializes the device within a short time. The demonstrated accelerated recovery behavior by the voltage spike gives the insight to estimate a real-time multimodal photo-detecting system in the novel framework of back-to-back Schottky junctions. The key for the system is the engagement of periodic voltage pulses (-2 to +5 V with a frequency of 1 Hz) to achieve the repetitive mode-switching and rapid

rise/decay times, simultaneously (Figure 3d). The time-resolved current under UV and visible lights are displayed in Figures 3e and 3f, respectively. The negative photocurrents (the direction of Al→ITO) were generated regardless of the irradiant wavelength, while the positive photocurrent (the direction of ITO→Al) selectively appeared only under the UV light, which quickly decayed as soon as turning the light off (Figure 3e). Both rise/decay times were less than 1 sec, which is a much shorter interval than those of existing dual-mode detectors (> 30 sec). Thus, it was substantiated that the platform is capable of tracking broadband light sources (from the negative current) and selectively extracting UV information (from the positive current) simultaneously. In addition, the superior repeatability of the suggested dual-mode detection system was confirmed by comparing the performance before and after 50 cycles of UV light pulses (5s on / 5s off) (Figure 3g).

The pivotal prerequisite to selective and precise digitization of UV light is a consistent responsivity of a visible-blind detector even under fluctuated visible light conditions. A visible-independent UV detection of the device was additionally explored by measuring the photocurrent under a visible and UV light combined light condition (Figure 4a). The time-resolved photocurrent was tracked under arbitrary light illumination consisting of triple UV light pulses and a single visible light pulse. The time-resolved photocurrent was tracked under arbitrary light illumination consisting of triple UV light pulses (irradiance of 0.5 mW cm<sup>-2</sup>) and a single visible light pulse (irradiance of 0.1 mW cm<sup>-2</sup>). Simultaneous irradiation of two lights increased negative photocurrent by 5% and 70%, compared to those under the single 365 and 625 nm source, respectively, whereas the positive photocurrent induced by the UV light was not affected in any way with or without visible light. As shown in Figure 4b, the selective photoresponse to UV light was still valid even under the high irradiance of visible light above 10 mW cm<sup>-2</sup>.

Furthermore, a spatial photocurrent mapping was conducted based on the single-pixel imaging system under a uniformly spread visible light (625 nm light), combined with a centralized UV light (365 nm) (Figure 4c). The photocurrent was measured in real-time while adjusting the position of the mobile stage supporting the device. From the overall red color distribution in the left panel of Figure 4c, it is identified that the negative current is sensitive to both visible and UV light. At the same time, the centralized positive photocurrent distribution with clear boundaries with the surrounding (non-UV region) shows at a glance that visible blind UV detection is also operational. Therefore, it has been proven that the system can conduct dual-mode detection simultaneously, regardless of the presence of visible light, which further emphasizes the applicability of the demonstrated system to a practical environment.

#### 4. Conclusion

Herein, we proposed a novel device configuration, named the dual Schottky junction (DSJ) detector, to realize UV-selective and broadband (UV+visible) light detection in a single device, excluding any additional filters or equipment. The pivotal block of the device was stacking two Schottky junctions in a form of the back-to-back diode configuration, enabling selective charge collection depending on bias direction and hence featuring the switchable spectral response. By anti-parallelly aligning n-IGZO/PEDOT and n-Si/PEDOT junctions, both broadband detection (UV-visible) and visible-blind UV detections were realized in a single device of which the functions were reversibly switchable according to bias polarity. Furthermore, the accelerated photoresponse/recovery rates were obtained by the application of a voltage pulse due to facilitated charge extraction. Consequently, the novel system successfully showcased both broadband and UV-selective light detection and mapped them onto a single frame without any dissipated filters. We believe that this study poses a new methodology for next-generation

photodetectors that are affordable, versatile, and highly Si-compatible, paving the way for

realizing a wide range of sensing applications (e.g., air pollution monitoring, oil spill detection,

and missile tracking systems) that require selective extraction of UV information from

broadband light sources.

ASSOCIATED CONTENT

Supporting Information. Empirical and theoretical UV-Vis reflectance; Investigation of TC<sub>G</sub>

values; EDS mapping images; HRTEM image; UV-Vis reflectance of the PEDOT/Si and

MoO<sub>3</sub>/PEDOT/Si samples; I-V curves of the PEDOT-free device; Responsivity and detectivity

of the DSJ device; Rise and decay times of the DSJ device. "This material is available free of

charge via the Internet at http://pubs.acs.org."

**AUTHOR INFORMATION** 

**Corresponding Author** 

\*Sunghwan Lee. Email: sunghlee@purdue.edu

**Author Contributions** 

S.L. and H.K. conceived the study. H.K. and R.M. prepared the devices. H.K., C.S.K., and J.P.

conducted material characterizations. H.K. performed the device characterization. S.L., B.-C. M.,

and H. K. analyzed the data and wrote the manuscript.

**Notes** 

The authors declare no competing financial interest.

**ACKNOWLEDGMENT** 

This work was partially supported by the U.S. National Science Foundation (NSF) Award No.

ECCS-1931088 and the Purdue Polytechnic RDE program.

17

#### **REFERENCES**

- (1) Yang, D.; Ma, D. Development of Organic Semiconductor Photodetectors: From Mechanism to Applications. *Adv. Opt. Mater.* **2019**, *7*, 1800522.
- (2) Konstantatos, G.; Sargent, E. H. Nanostructured Materials for Photon Detection. *Nat. Nanotechnol.* **2010**, *5*, 391–400.
- (3) Ye, W. N.; Xiong, Y. Review of Silicon Photonics: History and Recent Advances. *J. Mod. Opt.* **2013**, *60*, 1299–1320.
- (4) Yang, W.; Chen, J.; Zhang, Y.; Zhang, Y.; He, J.; Fang, X. Silicon-Compatible Photodetectors: Trends to Monolithically Integrate Photosensors with Chip Technology. *Adv. Funct. Mater.* **2019**, *29*, 1808182.
- (5) Li, Z.; Li, Z.; Zuo, C.; Fang, X. Application of Nanostructured TiO<sub>2</sub> in UV Photodetectors: A Review. *Adv. Mater.* **2022**, 2109083.
- (6) Chen, J.; Ouyang, W.; Yang, W.; He, J.; Fang, X. Recent Progress of Heterojunction Ultraviolet Photodetectors: Materials, Integrations, and Applications. *Adv. Funct. Mater.* 2020, 30, 1909909.
- (7) Xu, J.; Zheng, W.; Huang, F. Gallium Oxide Solar-Blind Ultraviolet Photodetectors: A Review. *J. Mater. Chem. C* **2019**, *7*, 8753–8770.
- (8) Guo, D.; Su, Y.; Shi, H.; Li, P.; Zhao, N.; Ye, J.; Wang, S.; Liu, A.; Chen, Z.; Li, C.; Tang, W. Self-Powered Ultraviolet Photodetector with Superhigh Photoresponsivity (3.05 A/W) Based on the GaN/Sn:Ga<sub>2</sub>O<sub>3</sub> Pn Junction. ACS Nano 2018, 12, 12827–12835.
- (9) Soci, C.; Zhang, A.; Xiang, B.; Dayeh, S. A.; Aplin, D. P. R.; Park, J.; Bao, X. Y.; Lo, Y. H.; Wang, D. ZnO Nanowire UV Photodetectors with High Internal Gain. *Nano Lett.* 2007, 7, 1003–1009.
- (10) Chen, H.; Liu, K.; Hu, L.; Al-Ghamdi, A. A.; Fang, X. New Concept Ultraviolet Photodetectors. *Mater. Today* **2015**, *18*, 493–502.
- (11) Zhao, Z.; Xu, C.; Niu, L.; Zhang, X.; Zhang, F. Recent Progress on Broadband Organic Photodetectors and Their Applications. *Laser Photon. Rev.* **2020**, *14*, 2000262.
- (12) Dhanabalan, S. C.; Ponraj, J. S.; Zhang, H.; Bao, Q. Present Perspectives of Broadband Photodetectors Based on Nanobelts, Nanoribbons, Nanosheets and the Emerging 2D Materials. *Nanoscale* **2016**, *8*, 6410–6434.

- (13) Bansal, S.; Prakash, K.; Sharma, K.; Sardana, N.; Kumar, S.; Gupta, N.; Singh, A. K. A Highly Efficient Bilayer Graphene/ZnO/Silicon Nanowire Based Heterojunction Photodetector with Broadband Spectral Response. *Nanotechnology* 2020, 31, 405205.
- (14) Chauhan, K. R.; Patel, D. B. Functional Nanocrystalline TiO2 Thin Films for UV Enhanced Highly Responsive Silicon Photodetectors. *J. Alloys Compd.* **2019**, *792*, 968–975.
- (15) Gao, T.; Zhang, Q.; Chen, J.; Xiong, X.; Zhai, T. Performance-Enhancing Broadband and Flexible Photodetectors Based on Perovskite/ZnO-Nanowire Hybrid Structures. *Adv. Opt. Mater.* **2017**, *5*, 1700206.
- (16) Samanta, C.; Bhattacharya, S.; Raychaudhuri, A. K.; Ghosh, B. Broadband (Ultraviolet to Near-Infrared) Photodetector Fabricated in n-ZnO/p-Si Nanowires Core—Shell Arrays with Ligand-Free Plasmonic Au Nanoparticles. *J. Phys. Chem. C* **2020**, *124*, 22235–22243.
- (17) Gomathi, P. T.; Sahatiya, P.; Badhulika, S. Large-Area, Flexible Broadband Photodetector Based on ZnS-MoS 2 Hybrid on Paper Substrate. *Adv. Funct. Mater.* **2017**, *27*, 1701611.
- (18) Wu, Z.; Jie, W.; Yang, Z.; Hao, J. Hybrid Heterostructures and Devices Based on Two-Dimensional Layers and Wide Bandgap Materials. *Mater. Today Nano* **2020**, *12*, 100092.
- (19) Wang, J.; Chen, S.-C.; Yin, Z.; Zheng, Q. Broadband Organic Photodetectors Based on Ternary Blend Active Layers with Enhanced and Spectrally Flat Response. *J. Mater. Chem. C* **2020**, *8*, 14049–14055.
- (20) Guo, F.; Yang, B.; Yuan, Y.; Xiao, Z.; Dong, Q.; Bi, Y.; Huang, J. A Nanocomposite Ultraviolet Photodetector Based on Interfacial Trap-Controlled Charge Injection. *Nat. Nanotechnol.* **2012**, *7*, 798–802.
- (21) Chen, H.; Liu, H.; Zhang, Z.; Hu, K.; Fang, X. Nanostructured Photodetectors: From Ultraviolet to Terahertz. *Adv. Mater.* **2016**, *28*, 403–433.
- (22) Sabnis, R. W. Color Filter Technology for Liquid Crystal Displays. *Displays* **1999**, *20*, 119–129.
- (23) Do, Y. S.; Park, J. H.; Hwang, B. Y.; Lee, S.-M.; Ju, B.-K.; Choi, K. C. Plasmonic Color Filter and Its Fabrication for Large-Area Applications. *Adv. Opt. Mater.* **2013**, *1*, 133–138.
- (24) Xie, Y.; Madel, M.; Li, Y.; Jie, W.; Neuschl, B.; Feneberg, M.; Thonke, K. Polaritiy-Controlled Ultraviolet/Visible Light ZnO Nanorods/p-Si photodetector. *J. Appl. Phys.* **2012**, *112*, 123111.

- (25) Um, H.-D.; Moiz, S. A.; Park, K.-T.; Jung, J.-Y.; Jee, S.-W.; Ahn, C. H.; Kim, D. C.; Cho, H. K.; Kim, D.-W.; Lee, J.-H. Highly Selective Spectral Response with Enhanced Responsivity of n-ZnO/p-Si Radial Heterojunction Nanowire Photodiodes. *Appl. Phys. Lett.* 2011, 98, 033102.
- (26) Mridha, S.; Basak, D. Ultraviolet and Visible Photoresponse Properties of n-ZnO/p-Si Heterojunction. *J. Appl. Phys.* **2007**, *101*, 083102.
- (27) Eastment, R. M.; Mee, C. H. B., Work function measuremens on (100), (110), and (111) surfaces of aluminium. *J. Phys. F: Metal Phys.* **1973**, *3*, 1738–1743.
- (28) Tsakiris, V.; Kappel, W.; Alecu, G., Solid state diffusion welding of Cu-Fe/Al/Ag and Al-Ni dissimilar metals. *J. optoelectron.*. *Adv. Mater.* **2011**, *13*, 1176–1180.
- (29) Yoosuf Ameen, M.; Pradhan, S.; Remyth Suresh, M.; Reddy, V. S. MoO3 Anode Buffer Layer for Efficient and Stable Small Molecular Organic Solar Cells. Adv. *Opt. Mater.* **2015**, *39*, 134–139.
- (30) Kim, H.-J.; Seo, K.-W.; Noh, Y.-J.; Na, S.-I.; Sohn, A.; Kim, D.-W.; Kim, H.-K. Work Function and Interface Control of Amorphous IZO Electrodes by MoO<sub>3</sub> Layer Grading for Organic Solar Cells. *Sol. Energy Mater. Sol. Cells* **2015**, *141*, 194–202.
- (31) Cattin, L.; Morsli, M.; Bernède, J. Improvement in the Lifetime of Planar Organic Photovoltaic Cells through the Introduction of MoO<sub>3</sub> into Their Cathode Buffer Layers. *Electronics* **2014**, *3*, 122–131.
- (32) Bai, Y.; Zhao, C.; Guo, Q.; Zhang, J.; Hu, S.; Liu, J.; Hayat, T.; Alsaedi, A.; Tan, Z. Enhancing the Electron Blocking Ability of N-Type MoO3 by Doping with p-Type NiO for Efficient Nonfullerene Polymer Solar Cells. *Org. Electron.* **2019**, *68*, 168–175.
- (33) Chang, S. H.; Lin, K.-F.; Chiu, K. Y.; Tsai, C.-L.; Cheng, H.-M.; Yeh, S.-C.; Wu, W.-T.; Chen, W.-N.; Chen, C.-T.; Chen, S.-H.; Wu, C.-G. Improving the Efficiency of CH3NH3PbI3 Based Photovoltaics by Tuning the Work Function of the PEDOT:PSS Hole Transport Layer. *Sol. Energy* **2015**, *122*, 892–899.
- (34) Nardes, A. M.; Kemerink, M.; de Kok, M. M.; Vinken, E.; Maturova, K.; Janssen, R. A. J. Conductivity, Work Function, and Environmental Stability of PEDOT:PSS Thin Films Treated with Sorbitol. *Org. Electron.* **2008**, *9*, 727–734.
- (35) Zhang, L.; Zhou, X.; Chang, B.; Wang, L.; Xiao, Y.; He, H.; Zhang, S. Source-Drain Resistance Characteristics of Back-Channel Etched Amorphous InGaZnO Thin Film

- Transistors with TiO 2:Nb Protective Layer. *Mater. Sci. Semicond. Process.* **2017**, *68*, 147–151.
- (36) Lee, H.; Lee, S.; Kim, Y.; Siddik, A. B.; Billah, M. M.; Lee, J.; Jang, J. Improvement of Stability and Performance of Amorphous Indium Gallium Zinc Oxide Thin Film Transistor by Zinc-Tin-Oxide Spray Coating. *IEEE Electron Device Lett.* **2020**, *41*, 1520–1523.
- (37) Cho, H.; Douglas, E. A.; Gila, B. P.; Craciun, V.; Lambers, E. S.; Ren, F.; Pearton, S. J. Band Offsets in HfO 2/InGaZnO 4 Heterojunctions. *Appl. Phys. Lett.* **2012**, *100*, 012105.
- (38) Burkhard, G. F.; Hoke, E. T.; McGehee, M. D. Accounting for Interference, Scattering, and Electrode Absorption to Make Accurate Internal Quantum Efficiency Measurements in Organic and Other Thin Solar Cells. *Adv. Mater.* **2010**, *22*, 3293–3297.
- (39) Li, Y.-T.; Han, C.-F.; Lin, J.-F., Characterization of the electrical and optical properties for a-IGZO/Ag/a-IGZO triple-layer thin films with different thickness depositions on a curved glass substrate. *Opt. Mater. Exp.* **2019**, *9*, 3414.
- (40) Tsay, C.-Y.; Huang, T.-T., Improvement of physical properties of IGZO thin films prepared by excimer laser annealing of sol-gel derived precursor films. *Physics* **2013**, *140*, 365–372.
- (41) Zheng, M.; Xu, Y.; Wang, X.; Zhang, G.; Li, W.; Jiang, L.; Zhang, L.; Wu, H.; Lin, Q.; Liu, C. ZnO-Based Ultraviolet Photodetectors with Tunable Spectral Responses. *Phys. status solidi Rapid Res. Lett.* 2019, 13, 1900441.
- (42) Esopi, M. R.; Zheng, E.; Zhang, X.; Cai, C.; Yu, Q. Tuning the Spectral Response of Ultraviolet Organic–Inorganic Hybrid Photodetectors *via* Charge Trapping and Charge Collection Narrowing. *Phys. Chem. Chem. Phys.* **2018**, *20*, 11273–11284.
- (43) Li, N.; Lim, J.; Azoulay, J. D.; Ng, T. N., Tuning the charge blocking layer to enhance photomultiplication in organic softwave infrared photodetectors. *J. Mater. Chem. C.* **2020**, *δ*, 15142–15149.
- (44) Vijayan, R. A.; Essig, S.; Wolf, S. D.; Ramanathan, B. K.; Löpper P., Ballif, C.; Varadharajaperumal, M., Hole-collection mechanism in passivating metal-oxide contacts on Si solar cells: Insights from numerical simulation. *IEEE Photon. Technol. Lett.* **2018**, *8*, 473–482.
- (45) Mudgal, S.; Nayak, M.; Singh, S.; Komarala, V. K., Study of anomalous S-shape in current density-voltage characteristics of carrier selective contact molybdenum oxide and

- amorphous silicon based heterojunction silicon solar cells. AIP Conf. Proc. 2019, 2147, 020009.
- (46) Wan, X.; Xu, Y.; Guo, H.; Shehzad, K.; Ali, A.; Liu, Y.; Yang, J.; Dai, D.; Lin, C.-T.; Liu, L.; Cheng, H.-C.; Wang, F.; Wang, X.; Lu, H.; Hu, W.; Pi, X.; Dan, Y.; Luo, J.; Hasan, T.; Duan, X.; Li, X.; Xu, J.; Yang, D.; Ren, T.; Yu, B. A Self-Powered High-Performance Graphene/Silicon Ultraviolet Photodetector with Ultra-Shallow Junction: Breaking the Limit of Silicon? npj 2D Mater. Appl. 2017, 1, 4.
- (47) Chen, X.-X.; Xiao, X.-H.; Shi, Z.-F.; Du, R.; Li, X.-J. Self-Powered Ultraviolet Photodetection Realized by GaN/Si Nanoheterostructure Based on Silicon Nanoporous Pillar Array. *J. Alloys Compd.* **2018**, *767*, 368–373.
- (48) Song, W.; Wang, X.; Chen, H.; Guo, D.; Qi, M.; Wang, H.; Luo, X.; Luo, X.; Li, G.; Li, S. High-Performance Self-Powered UV-Vis-NIR Photodetectors Based on Horizontally Aligned GaN Microwire Array/Si Heterojunctions. *J. Mater. Chem. C* **2017**, *5*, 11551–11558.
- (49) Ji, T.; Liu, Q.; Zou, R.; Zhang, Y.; Wang, L.; Sang, L.; Liao, M.; Hu, J. Enhanced UV-Visible Light Photodetectors with a TiO 2/Si Heterojunction Using Band Engineering. *J. Mater. Chem. C* **2017**, *5*, 12848–12856.
- (50) Kim, D. C.; Jung, B. O.; Lee, J. H.; Cho, H. K.; Lee, J. Y.; Lee, J. H. Dramatically Enhanced Ultraviolet Photosensing Mechanism in a N-ZnO Nanowires/i-MgO/n-Si Structure with Highly Dense Nanowires and Ultrathin MgO Layers. *Nanotechnology* 2011, 22, 265506.
- (51) Tian, W.; Lu, H.; Li, L. Nanoscale Ultraviolet Photodetectors Based on Onedimensional Metal Oxide Nanostructures. *Nano Res.* **2015**, *8*, 382–405.
- (52) Hsu, C.-L.; Chang, S.-J. Doped ZnO 1D Nanostructures: Synthesis, Properties, and Photodetector Application. *Small* **2014**, *10*, 4562–4585.
- (53) Kim, H.; Kim, W.; Park, J.; Lim, N.; Lee, R.; Cho, S. J.; Kumaresan, Y.; Oh, M.-K.; Jung, G. Y. Surface Conversion of ZnO Nanorods to ZIF-8 to Suppress Surface Defects for a Visible-Blind UV Photodetector. *Nanoscale* 2018, 10, 21168–21177.

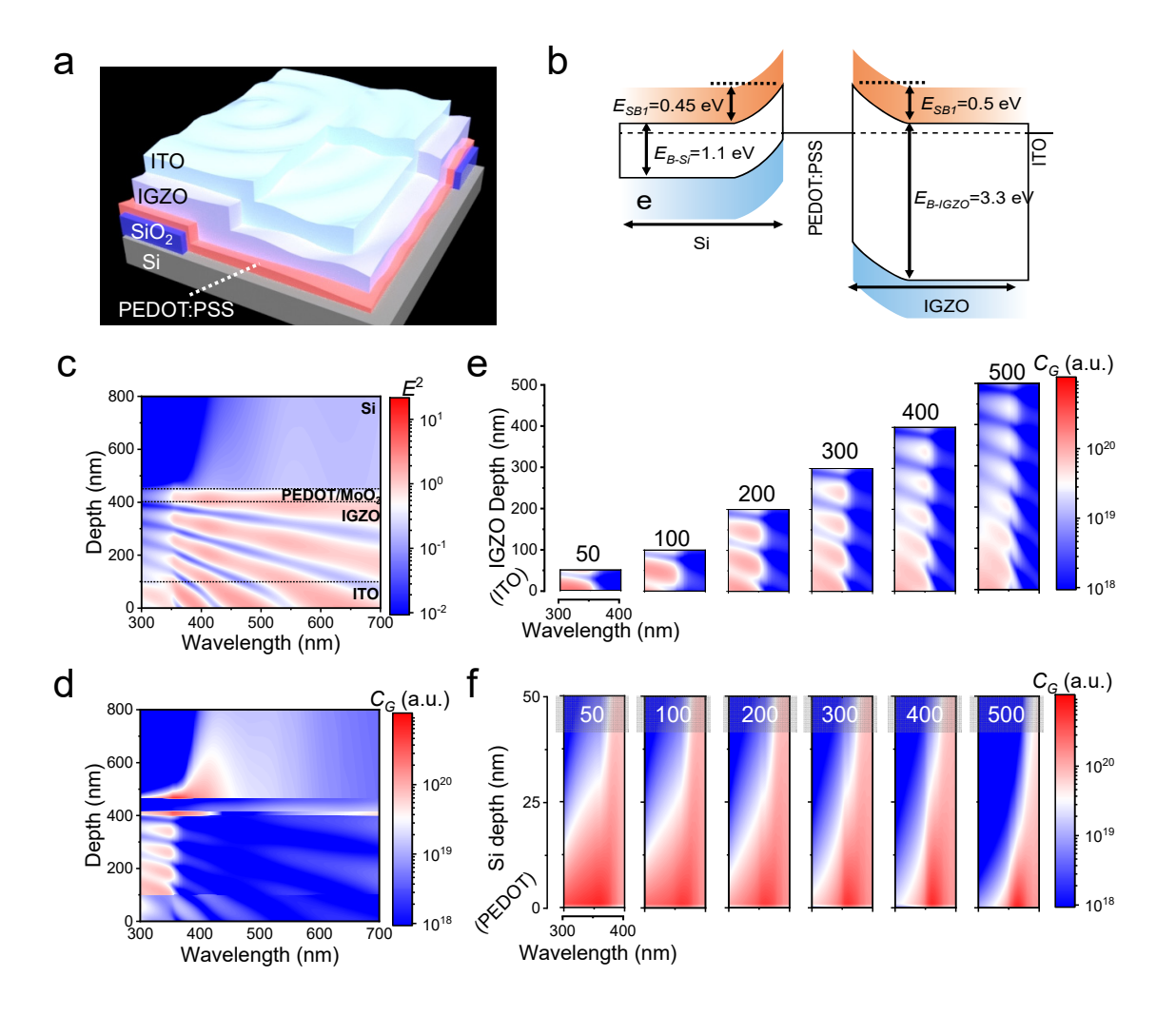


**Figure 1.** Device configuration and simulated optical properties of the DSJ device. (a) Schematic of the DSJ device. (b) Energy band diagram of the DSJ device with two Schottky junctions. (c-f) Simulation results of the optical field and charge-generation rate  $(C_G)$ . (c) Optical field profile and (d)  $C_G$  distribution of the DSJ device with the 300 nm-thick IGZO layer. (e)  $C_G$  distribution in the IGZO layer and (f) the Si layer under UV illumination (300-400 nm) with different IGZO thicknesses. The bottom layer (depth of 0 nm) of the (e) and (f) denotes a boundary of the IGZO/ITO and Si/PEDOT interface, respectively. For the Si layer in (f), the first 50 nm is selectively depicted to clear the difference at a glance.

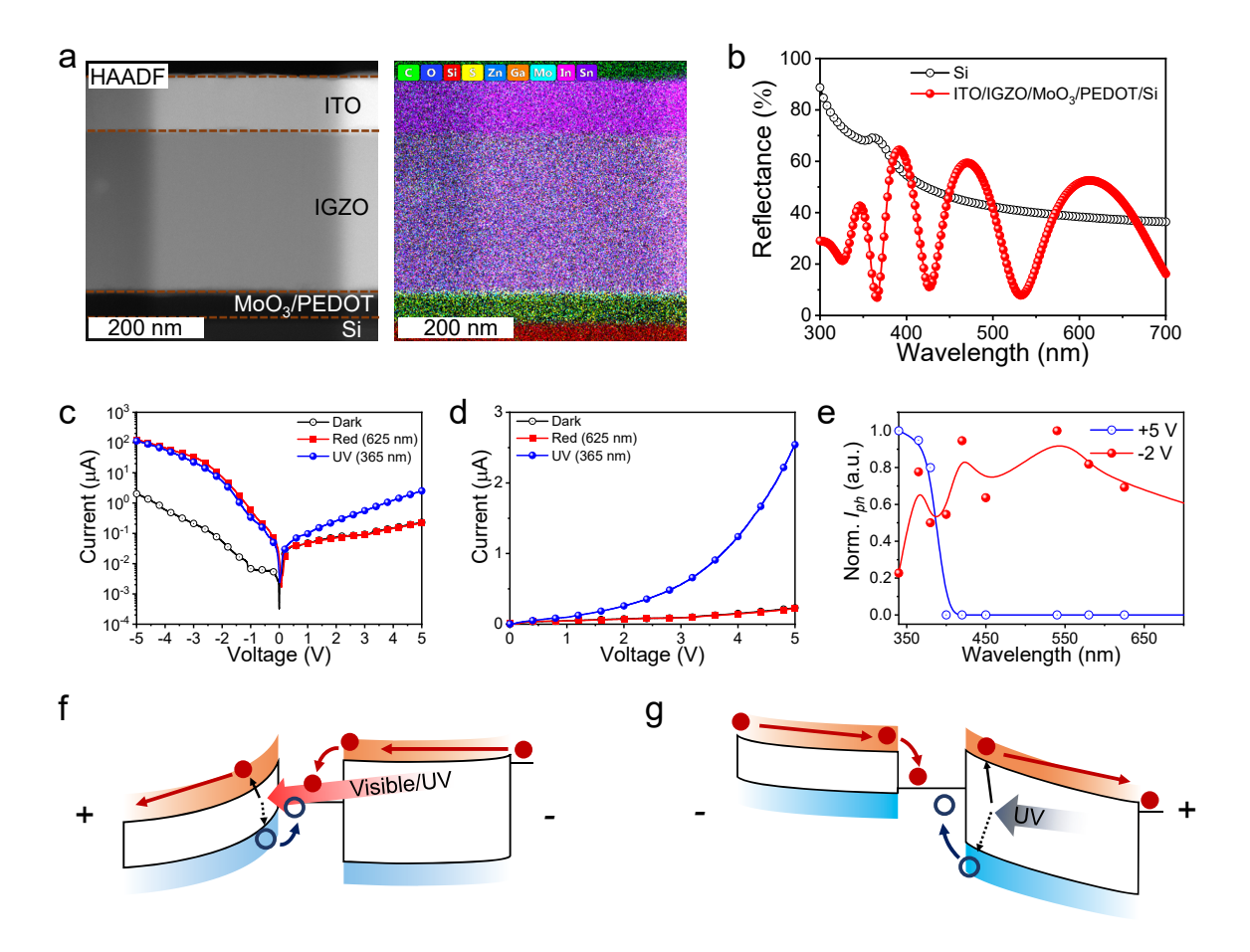


**Figure 2.** Device characterization and working mechanism. (a) HAADF-STEM (left) and its corresponding EDS mapping image (right). (b) Optical reflectance of the DSJ device. (c-d) *I-V* curves of the DSJ device with and without light illuminations (625 nm or 365 nm LED with an irradiance of 1 mW cm<sup>-2</sup>). The linear scale plot for the forward bias regime is in (d). (e) Normalized photocurrents under different wavelength lights. Blue and red spectral lines represent the spectral curve recorded at +5 and -2 V, respectively. (f,g) Schematic representing the underlying principle of the dual-spectral detecting behavior of the DSJ device.

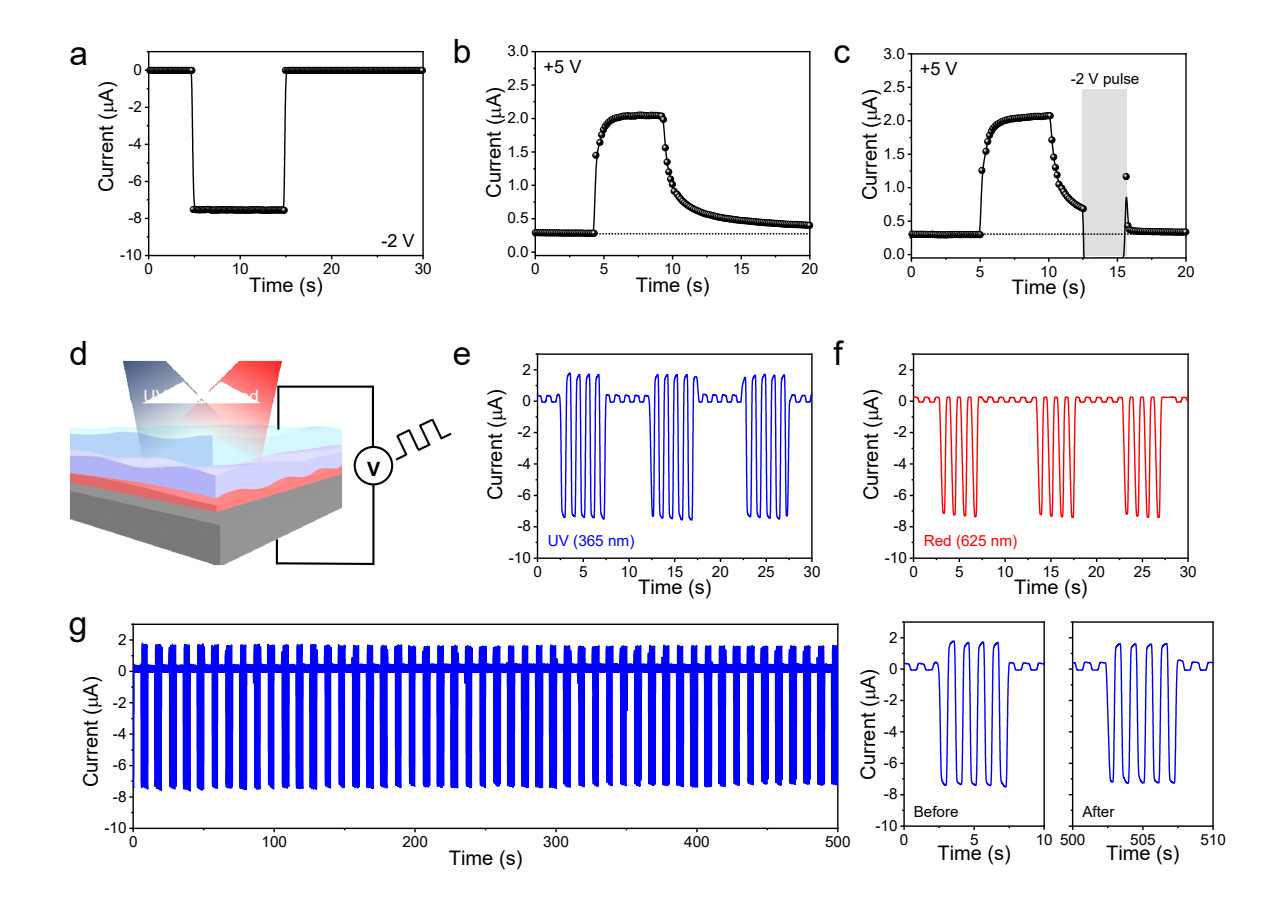


**Figure 3.** Dual-mode light detection, assisted by an engagement of pulsed voltage. Time-resolved photocurrents recorded at (a) -2 V and (b) +5 V. (c) Time-resolved photocurrent at +5 V with a negative spike which accelerates the recovery. (d) Schematic of dual-mode light detection assisted by the voltage pulses. (e-g) Time-resolved photocurrent measurement at a 1 Hz of voltage-pulse. Recorded photocurrent under (e) UV and (f) red light illumination. (g) Repeatability test of the DSJ device. The last two panels in (g) represent the photoresponse curve before and after 50 UV light pulses, respectively.

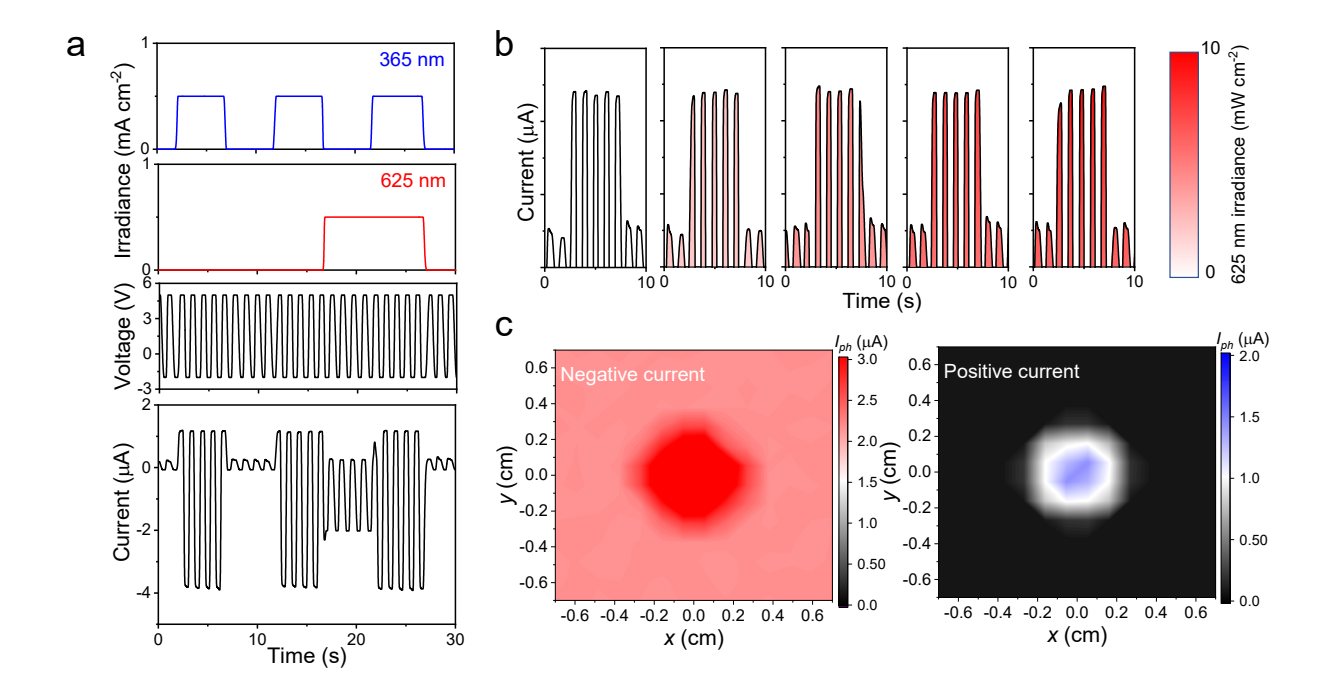


**Figure 4.** Visible-blind UV detection. (a) Time-resolved photocurrent under mixed light conditions. (b) Positive photocurrents under the same UV light with different 625 nm light irradiance. (c) Spatial photocurrent mapping result. The illuminated condition consisted of diffused 625 nm LED and centralized 365 nm light. The left and right maps represent the negative and positive peak currents, respectively.

### **Table of Contents (TOC)**

